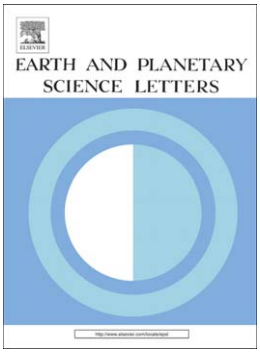

Non-Newtonian rheology of crystal-bearing magmas and implications for magma ascent dynamics

Luca Caricchi, Luigi Burlini, Peter Ulmer, Taras Gerya, Melissa Vassalli, Paolo Papale

PII: S0012-821X(07)00598-5
DOI: doi: 10.1016/j.epsl.2007.09.032
Reference: EPSL 8925

To appear in: *Earth and Planetary Science Letters*

Received date: 11 June 2007
Revised date: 6 September 2007
Accepted date: 21 September 2007

Please cite this article as: Luca Caricchi, Luigi Burlini, Peter Ulmer, Taras Gerya, Melissa Vassalli, Paolo Papale, Non-Newtonian rheology of crystal-bearing magmas and implications for magma ascent dynamics, *Earth and Planetary Science Letters* (2007), doi: 10.1016/j.epsl.2007.09.032

Non-Newtonian rheology of crystal-bearing magmas and implications for magma ascent dynamics

Luca Caricchi [a, *], Luigi Burlini [a], Peter Ulmer [a], Taras Gerya [a], Melissa Vassalli [b, c], Paolo Papale [b]

[a] Department of Earth Sciences, ETH Zurich, Clausiusstrasse 25, CH-8092, Zurich, Switzerland

[b] Istituto Nazionale di Geofisica e Vulcanologia, Via della Faggiola 32, 56126 Pisa, Italy

[c] Physics Department, Università di Bologna, Via Berti Pichat 6/2, 40127 Bologna, Italy

[*] Corresponding author: Tel. +41 44 632 78 24; fax: +41 44 632 16 36; e-mail address: luca.caricchi@erdw.ethz.ch

Abstract

The eruptive dynamics of volcanic systems are largely controlled by the viscosity of deforming magma. Here we report the results of a series of high-temperature, high-pressure experiments at conditions relevant for volcanic conduits (250 MPa confining pressure and temperature between 500 °C and 900 °C) that were undertaken to investigate the rheology of magma with crystal fractions varying between 0.5 and 0.8 (50 to 80 wt. %) at different strain-rate conditions. The experiments demonstrate that the presence of crystals increases the relative viscosity (ratio between the viscosity of the mixture and the viscosity of the melt phase) of magmas and additionally induces a decrease of the relative viscosity with increasing strain-rate (shear thinning, non-Newtonian behavior). The experimental results, combined with existing data at low crystal fractions (0 - 0.3), were used to develop a semi-empirical parameterization that describes the variations of relative viscosity for crystal fractions between 0 and 0.8 and accounts for the complex non-Newtonian rheology of crystal-bearing magmas.

The new parameterization, included into numerical models simulating the magma ascent dynamics, reveals that strain-rate - dependent rheology significantly modifies the dynamic behavior inside volcanic conduits, particularly affecting the magma fragmentation conditions.

Keywords: Magma rheology, experimental deformation, Non-Newtonian rheology, conduit-flow dynamics, fragmentation

1. Introduction

The volcanic eruption dynamics are intimately related to the rheological behavior of magma [1]. The knowledge of the rheology of such materials is therefore prerequisite for volcanic hazard assessment, as it directly contributes to the eruptive behavior of volcanic systems. Magma consists of a mixture of a silicic liquid, crystals and gases and the flow behavior of magmatic mixtures is ultimately determined by the presence of these different components. While magmas have been extensively investigated with respect to the solubility of gases, viscosity of the melt fraction and the rheological effect of gas bubbles [e.g. 2-5], an equation able to account for the influence of crystals on magma rheology is still unavailable. The simplifying assumption of pseudo-fluid Newtonian behavior (viscosity not depending on strain-rate, $\dot{\gamma}$) implemented in numerical models designed to simulate volcanic eruption [6-8], could indeed induce significant errors in the estimation of the flow dynamics inside the conduit.

We have, therefore, conducted a series of experiments on a water bearing (2.7 wt. % H_2O) rhyolitic melt containing quartz particles, which closely represents a magma rising inside a volcanic conduit, employing different crystal fractions, temperature and strain rate conditions to study potential non-Newtonian effects related to the presence of crystals. Our experimental results are combined with literature data obtained for low solid-fraction materials [9] and used to constrain a system of equations that account for the variations of η_r (ratio between the viscosity of the mixture and the viscosity of the suspending liquid phase) over a wide range of crystal fractions ϕ (0-0.8) and strain-rates (10^{-7}-$10^{0.5}$ s^{-1}). By introducing these equations in the numerical model described by Papale et al. [10], which considers the variations of the physical properties of magma

64 during flow in the volcanic conduit (e.g. decompression induced exsolution of volatiles,
65 variations of densities, presence of bubbles in the mixture), the effect of crystals on the
66 conduit dynamics of magmas can adequately be quantified.
67 The new set of equations provides two principal advances for volcanic eruption
68 modeling: (1) the possibility to simulate eruptions of crystal-rich magmas (ϕ>0.4) that are
69 characteristic of highly explosive eruptions, such as for example the eruptions of the Fish
70 Canyon Tuff [11], the 1631 BC eruption of Mount Vesuvius [12] or the 1991 eruption of
71 Pinatubo [13]. In the past, it was very difficult to perform appropriate simulations of
72 these volcanic eruptions due to the lack of equations describing η_r of magmas containing
73 such high crystal volume fractions. (2) In addition, the new set of equation provides an
74 adequate description of the complex $\dot{\gamma}$-dependent rheology of natural magmas that can
75 now be taken into account in numerical simulations of magma flow dynamics.
76

77 **2. Experimental procedure**

78 *2.1 Sample preparation*

79 Powdered oxides and hydroxides were thoroughly mixed to obtain a fine-grained powder
80 of haplogranitic composition (Online material, Table 1), containing 2.7 wt. % H_2O added
81 as AlO(OH) and $Al(OH)_3$. These two hydroxides were mixed in appropriate proportions
82 to balance the Al_2O_3 and H_2O content of the glass. The powdered mixture was melted for
83 24 hours in a large volume-internally heated pressure vessel at 1100 °C and 180 MPa,
84 producing approximately 1 kg of homogeneous glass (confirmed by electron microprobe
85 analysis, Online material, Table 1). The H_2O content of the glass was verified after
86 synthesis by FTIR (Fourier Transform infrared spectroscopy) at LMU-University of

87 Munich and resulted 2.7±0.1 wt. % H_2O. The equilibrated glass was subsequently ground
88 to a very fine grain-size powder (2-4 μm) and mixed with appropriate proportions of
89 crushed quartz to obtain the desired crystal fractions (ϕ). The quartz particles were sieved
90 and the grain size class between 65 and 125 μm was selected. The mixtures of particles
91 and glass were subsequently hot-isostatically pressed (HIP) at 250 MPa and 800 °C for 1
92 hour to re-melt the glass and remove the porosity. Cylindrical specimens of about 1.8 cm^3
93 were drilled from the hot pressed material. The chemically and texturally homogeneous
94 material contained neither visible gas bubbles nor crystal-clusters. The particular
95 compositions of starting materials were selected because the viscosity of the melt phase is
96 well known [e.g. 14] and the system is chemically very stable. The very steep slope of the
97 quartz-liquidus surface in the ternary quartz-albite-orthoclase system for the pressure-
98 temperature range investigated minimizes the amount of reactions between melt and
99 suspended quartz-grains during the course of the deformation experiments. Electron
100 microprobe analyses of the glasses conducted before and after the experiments with
101 duration between 1 and 6 hours, revealed insignificant variations in glass composition
102 (ΔSiO_2=-0.09, ΔAl_2O_3=+0.16, ΔNa_2O=-0.37, ΔK_2O=-+0.31; all within standard
103 deviation of multiple analyses; Online material, Table 1). For the purposes of this work,
104 chemical stability of the investigated system is fundamental because it allows rigorous
105 control on the degree of crystallinity and on the viscosity of the suspending liquid.
106 Chemical reaction would produce variations in the degree of crystallinity and in the
107 viscosity of the liquid, thereby inducing significant errors in the resulting values of η_r.
108 For these reasons we favored synthetic samples over natural materials. The viscosities of

the haplogranitic melt at different temperatures were estimated using the equations reported in [14] and [15].

2.2 Experimental methods and apparatus

All experiments were conducted in a high-temperature, high-pressure internally heated Paterson-type deformation apparatus [16] at 250 MPa confining pressure and temperatures varying between 500 and 900 °C. The sample diameter for all experiments was 12 mm; the sample length varied between 4 and 5 mm in torsion and between 12 and 15 mm in uniaxial compression tests. The cylindrical specimens are placed between alumina cylinders that transmit the differential stress on the sample. The assembly is composed of 4 alumina cylinders, 2 on each side used to transmit the differential stress to the sample, and two alumina spacers that are used to separate the transmitting cylinders from direct contact with the partially molten sample. Temperature is measured by a shielded K-type (Chromel – Alumel) thermocouple at the top of the upper spacer that is 3 mm thick. The temperature difference along the entire sample length does not exceed 2 K. The entire sample assembly is inserted in an iron tube in order to isolate the sample from the confining argon gas. The resolution of the load cell is 1 Nm in torsion [16, 17] and 1 kN in compression, which induces uncertainties in reported stress values of 3 MPa and 5 MPa respectively (Table 1).

2.3 Carrying out the deformation experiments

Torsion and compression experiments were performed at constant strain-rates (Fig. 1) that varied between $1 \cdot 10^{-6}$ and $1 \cdot 10^{-4}$ s^{-1} in torsion and up to $1 \cdot 10^{-3}$ s^{-1} in compression

132 configuration. In the case of torsion experiments, the relation between torque (applied
133 force given by the reading of the internal load cell of the apparatus) and stress is
134 dependent on the stress exponent (n) of the material under investigation [16]. In the
135 experiments reported here, the n-values for comparable ranges of strain rate were similar
136 for all crystal fractions (Table 1; Fig. 1 Online material). The appropriate n values
137 required to convert the torque in stress were selected from logarithmic plots displaying
138 the maximum torque versus strain rate. In such a plot the slopes of the fitting lines for
139 different torque values correspond to the stress exponent (Fig. 1 Online material). Total
140 strain reached up to gamma 0.8 in torsion (shear strain [16]) and 20 % shortening in
141 compression configuration. Two to three deformation tests were performed for each
142 different degree of solid fractions (0.5, 0.6, 0.7 and 0.8) to investigate the effect of
143 variable temperatures and to cover a wide range of strain rates.
144 Several experiments were repeated at the same strain-rate to evaluate the reproducibility
145 in peak stress that resulted within 5 MPa (e.g. Fig. 1, ϕ=0.6, T=600°C) that converts to an
146 average error in viscosity of about 0.05 log units. Stepping strain rate tests, i.e. increasing
147 the strain rate in a stepwise manner, were only conducted after steady state stress
148 conditions were achieved for a given strain rate (Fig. 1a). The stress values presented in
149 Table 1 are corrected for the strength of the iron jacket applying the flow law reported by
150 Frost et al. [18] that is in accordance with calibrations performed in our laboratory by
151 Barnhoorn et al. [17], and that is also favored by Rutter et al. [19]. This correction results
152 in a decrease of the viscosities between 0.2 and 0.01 log units compared to the raw data
153 for the lowest and the highest stresses measured respectively. The presence of the iron
154 jacket and the resolution of the load cell allow accurate measurements of the viscosity for

values higher than 10^9 Pa·s. In fact, an applied stress of 3 MPa corresponding to the resolution of the internal load cell in torsion configuration at $1 \cdot 10^{-3}$ s^{-1} shear rate, results an apparent viscosity of $10^{9.5}$ Pa·s. In order to obtain viscosities larger than 10^9 Pa·s for all our samples, the temperatures of the experiments had to be adjusted as a function of the solid fraction (500 °C for ϕ=0.5, 600 °C for ϕ=0.6, 850 °C for ϕ=0.7 and 900 °C for ϕ=0.8). In order to compare strain rates and stresses from torsion and compression experiments, uniaxial strain rate and stress values were converted to shear strain-rates and shear stresses using the conversion laws 38 - 42 reported in [16]. Compression and torsion experiments performed at similar strain rate, ϕ and temperature compare well in terms of peak stresses (e.g at ϕ=0.7 and T=850 °C, Fig. 1).

3. Experimental results

All torsion and compression experiments exhibit identical behavior of an initial linear increase of stress with strain (elastic behavior), followed by a yielding stage and finally flow at a constant value of stress (Fig. 1a). The elastic response of the sample was restricted to a relatively short interval of strain, followed by longer, progressively decreasing strain-hardening (stress increase with respect to strain) until flow at constant stress was attained. The strain-hardening phase extended over a larger strain interval in torsion than in compression tests for comparable strain rates (e.g. at ϕ=0.7 and T=850 °C, Fig. 1a). Values reported in Table 1 represent the maximum stress attained for the applied strain-rate during the flow stage. The stress and strain rate values were used to calculate the apparent viscosity (Eq.1):

$$\eta_{app} = \tau / \dot{\gamma} \quad (1)$$

where τ is the peak shear stress and $\dot{\gamma}$ is the corresponding shear rate (Fig.1 b).

In order to test if strain could affect the rheology of the investigated material, we performed several experiments (e.g. ϕ=0.6 and T=600°C; Fig. 1a and b) where the sample was unloaded after a series of strain stepping tests and subsequently reloaded applying a previously used strain rate. No variations were observed in the peak stress and thus in the resulting viscosity of the material (Fig. 1a and b) testifying to the absence of thixotropic behavior (variation of viscosity with the increase of applied strain).

3.1 Effect of temperature

The strength of the samples decreased with increasing temperature (Fig. 1a, ϕ=0.7 T=850 °C and T=800 °C): A 50 °C temperature increase leads to a decrease of the viscosity of approximately 0.2 log units. However, the same temperature increase results in a viscosity decrease of 0.4 log units for the pure melt phase [14, 15]. This difference indicates that for such high crystal fractions the rheological behavior of the system is controlled by both, the viscosity of the melt and the interactions between the suspended particles.

3.2 Effect of crystal fraction

The effect of the crystal fraction can be evaluated by comparing the stresses and apparent viscosities of experiments performed on samples with ϕ=0.7 and 0.8 at 850°C temperature (Fig.1 a): An increase of the solid fraction by 0.1 induces a considerable increase in the peak stress values, which results in an increase of the apparent viscosity of 0.6-0.7 log units (Fig. 1a and b, Table 1). In order to separate the effects of temperature and the effects of crystal fraction on the viscosity we plot the relative viscosity (η_r) of the

samples for the different solid fractions (Fig. 2). The relative viscosity is given as:

$$\eta_r=\eta_{app}/\eta_{melt} \quad (2)$$

where η_{app} is the measured apparent viscosity of the sample and η_{melt} is the viscosity of the suspending melt phase at a given temperature. η_r is therefore independent of temperature, because the change in temperature induces only a change in the viscosity of the suspending melt that is implicitly included in the definition of the relative viscosity. The increase of suspended solid fraction produces an increase of the relative viscosity (Fig. 2) that is particularly dependent on solid fraction between ϕ=0.5 and ϕ=0.7. The ϕ where viscosity starts to increase exponentially is defined as the "maximum packing fraction" of the system (ϕ_{max}; [20]). This parameter is dependent on several factor related to crystal size, shape, distribution and orientation [21, 22, 23]. The lines displayed in Figure 2 represent the results of the fitting procedure outlined in detail in Section 5.

3.3 Effect of strain rate

In all experiments viscosity was independent from strain rate for values lower than 10^{-5} s^{-1} i.e. Newtonian behavior was observed (Fig. 1b). Above this threshold, an increase of strain rate always induced a decrease of viscosity (Fig. 1b); this behavior is defined as "shear thinning" [e.g. 5] and is an expression of non-Newtonian behavior. Note that shear thinning results in an increase of ϕ_{max} (Fig. 2) with increasing strain rate.

The effects of strain rate on the relative viscosity are highlighted in Figure 3a.

The magnitude of decrease of relative viscosity is directly proportional to ϕ. Figure 3b displays the logarithmic value of η_r (relative viscosity) for any given value of strain rate normalized to the logarithmic value of η_r at low strain rates (i.e. in the Newtonian field).

This normalization allows evaluation of the relative effects of shear thinning on the relative viscosity. Figure 3a and 3b reveal that the *absolute magnitude of decrease* of the relative viscosity is higher for the higher crystal fractions, whereas the *relative decrease* of η_r is higher for lower crystal fractions of ϕ=0.5 and ϕ=0.6.

The principal experimental results can be summarized as follows:

1. In all experiments flow at constant value of stress and absence of strain weakening was observed.
2. Strain did not influence the rheology of the samples implying the absence of thixotropic behavior.
3. The relative viscosity (η_r) increased by about 5 orders of magnitude with increasing solid fractions (quartz crystals) from 0.5 to 0.8 (Fig. 2).
4. Two different dependencies of apparent viscosity from the strain-rate corresponding to Newtonian and non-Newtonian behavior (Fig. 3a and b) were observed. The Newtonian regime is characteristic for low strain-rates and the apparent viscosity in this regime is independent of the strain-rate (although it depends on solid fraction). In the non-Newtonian regime the apparent viscosity decreases with increasing strain-rate (shear thinning behavior).
5. The absolute magnitude of the apparent viscosity decrease is larger for larger solid fractions (Fig. 3a). However, the relative magnitude (i.e. log η_r/ log $\eta_{r(Newtonian),}$ of the shear thinning-induced decrease of viscosity is larger for lower solid fractions (ϕ=0.5 to ϕ=0.6, Fig. 3b).

The experiments, thus, imply that the introduction of solid particles into a viscous liquid results in two principal rheological effects: (i) increase of relative viscosity of

247 the suspension with increasing solid fraction, and (ii) the enhancement of non-
248 Newtonian behavior.

249 *3.2. Microstructures*

250 The microstructures generated during the deformation experiments were analyzed by
251 back scattered electron (BSE) imaging of polished sections cut through the recovered,
252 deformed samples (Fig. 4). Investigated samples from torsion experiments were cut out
253 from the external portion of the specimens, with the short axis parallel to the cylinder
254 axis, where simple shear geometry is best appreciated and shear is maximal [16].
255 Samples deformed in uniaxial compression were cut along the centre, parallel to the
256 cylinder axis. In all experiments (torsion and compression) planar features were
257 observed. However, we concentrate our discussion on the microstructures obtained in
258 torsion experiments, because, for the aspect ratio of the samples deformed in compression
259 (1-1.25), the internal stress is not homogeneously distributed and this renders the
260 interpretation rather complicated [24].

261 The planar features are oriented at about 30° and 150° with respect to the shear plane.
262 These features were observed in all deformed specimens and their geometry is
263 independent of the total strain applied. These bands are highlighted in Figure 4 by arrows
264 and consist of melt and crystals elongated parallel to the planar structures. The crystals in
265 these clusters have average grain sizes that are smaller than in the rest of the sample. The
266 thickness of these bands appears to correlate inversely with the crystal fraction (i.e. the
267 higher the crystal fraction the thinner the bands).

268 Comparable planar features have previously been observed in torsion experiments
269 conducted by Holtzman et al. [25] at higher ϕ (0.94-0.96). They used a viscous energy

dissipation function to argue that the minimum of total work required to produce deformation is obtained for angles of the localization bands of 25° with respect to the shear plane.

4. Discussion on the effects of crystals on magma rheology

Previous studies have shown that very different types of solid-liquid suspensions regarding composition (e.g. hard sphere colloidal suspensions or lithium disilicate melt plus lithium disilicate crystals) and fraction of suspended solid particles ($0.1 \leq \phi \leq 0.8$ [19, 20, 26-32]) display very similar dependence of the relative viscosity (η_r) on ϕ and $\dot{\gamma}$:

The relative viscosity η_r increases with ϕ in a sigmoidal fashion (Fig. 2). With increasing strain rate solid-liquid suspensions can display Newtonian, non-Newtonian and Binghamian behavior [20, 27-29, 32]. At relatively low strain rates ($<10^{-5}$ s^{-1}; [27, 30] and from this study, Fig. 3a and b) the behavior is Newtonian. An increase of strain rate induces shear thinning (non-Newtonian behavior) where the viscosity decreases until a minimum value is reached (Fig. 3). This minimum represents the onset of Binghamian behavior, which is characterized by a viscosity that is lower than the Newtonian viscosity but likewise independent from the strain rate. Here the definition of Binghamian behavior is not strictly related to the presence of yield strength but refers to the independence of the viscosity from the strain rate. In our experiments, the Binghamian behavior was not reached but only approached (Fig. 1a and b) due to the limitation of the maximum strain rates (10^{-3} s^{-1}) attainable. However, the existence of this rheological behavior at high $\dot{\gamma}$ has clearly been demonstrated previously [20, 27, 28, 31, 32]. In the Binghamian region a value of "fictive yield strength"(τ_0) can be obtained by linear extrapolation of the flow

293 stress values at high strain rate to zero strain rate (the principle is illustrated in the Inset in
294 Fig. 1a). τ_0 can be associated to the stress value at which macroscopic deformation starts
295 in the material, for this reason it could be interpreted as a yield strength that is strongly
296 dependent on crystal fraction and temperature. The values of fictive yield strength at the
297 conditions of the experiments are reported in Table 1. The flow law results a linear
298 decrease of stress with respect to strain rate at high deformation rates ($>10^{-4}$ s^{-1}
299 Binghamian behavior). For intermediate strain rates (10^{-4}-10^{-5} s^{-1} non-Newtonian
300 behavior) the stress decreases exponentially. For strain rates lower than 10^{-5} s^{-1} the stress
301 decreases linearly towards zero (Newtonian behavior) (Inset Fig. 1a).
302 Viscous heating is unable to account for the large decrease of viscosity (1-2 orders of
303 magnitude) observed in our experiments: The strain rates and the dimensions of the
304 specimens are far too low to induce a substantial production of heat and, consequently, a
305 considerable thermal gradient between the sample and the thermocouple used to control
306 the temperature during the experiments. In case the temperature would rise, the
307 thermocouple would register this temperature increase and the temperature-controller
308 would readjust the power output to bring the temperature immediately back to the target
309 value. Considering the maximum measured viscosity (~10^{13} Pa·s) and an applied strain
310 rate of $5 \cdot 10^{-6}$ s-1 (e.g. f=0.8; T=850°C; Table 1), the heat production per unit time would
311 result in $1 \cdot 10^{-2}$ K/s. Taking in account thermal diffusivity for silicic magmas as reported
312 in [33], viscous heating would not produce any appreciable (0.01 °C) gradient between
313 the centre of the sample and the thermocouple located at a distance of 8 mm from the
314 center of the sample (5 mm half specimen length and 3 mm spacer). Increasing the strain
315 rate in our experiment to $1 \cdot 10^{-4}$ s^{-1} we observed a decrease of viscosity to 10^{12} Pa·s. If we

repeat the same calculations, keeping the viscosity constant at the highest observed value of 10^{13} Pa·s and applying a strain rate $1 \cdot 10^{-4}$ s^{-1}, this would induce a maximum temperature increase of 3 °C after about 180 seconds corresponding to a decrease in viscosity of 0.03 log units. For longer periods, the temperature will be constant over the entire sample length and the temperature will be adjusted by the furnace to a constant value of 850°C.

We would like to emphasize that we have chosen temperature and $\dot{\gamma}$ conditions that keep the melt phase in the "relaxed" Newtonian region [5]. For these reasons, the observed shear thinning effects can exclusively be attributed to the presence of the solid quartz particles. This, in turn, implies that the presence of particles induces non-Newtonian behavior in temperature and strain rate ranges where the suspending medium itself behaves Newtonian.

4.1. Flow mechanics of crystal-bearing magmas

The visco-plastic deformation of magmas with ϕ up to 0.8 is due to the flow of the melt phase and consequently the plastic deformation of the suspended particles is negligible [19, 34]. This implies that the suspended particles move passively in response to the flow of the melt phase.

In order to understand the mechanics of magma deformation it is fundamental to reconcile the micro-structural observations and the rheological data:

a) It has been demonstrated that the micro-structural ordering (redistribution of melt and crystals) coincides with the transition from Newtonian to shear thinning and finally to

Binghamian behavior with increasing strain rate (Fig. 5a) for hard-sphere, relatively diluted, colloidal suspensions and for silicate melt suspensions with $\phi<\phi_{max}$ ($0.1<\phi<0.6$; [27, 28, 31, 32, 35, 36]). In this range of crystal fractions the application of relatively high stress (or high strain rates) leads to the generations of particles aggregates, which align according to the flow directions ([36]; Fig. 5a). A lower limit of stress or strain rate has to be overcome before these structures generate; this threshold corresponds to the transition from Newtonian to non-Newtonian (shear thinning) behavior. The alignment produces a smaller disturbance of the melt flow lines relative to a system that contains randomly distributed particles (Fig. 5a). The occurrence of a viscosity minimum obtained at high strain rates via shear thinning reflects the presence of a Binghamian region that corresponds to the attainment of the maximum or optimum possible ordering in the system (Fig. 5a).

b) For $\phi>\phi_{max}$ the deformation mechanisms are different than far more dilute suspensions because the suspended particles are in reciprocal contact. The flow in such material is, therefore, only possible if a certain amount of dilation occurs, which allows the particles to move relative to each other. The relationships between experimental data and mechanics of deformation for concentrated suspension ($\phi>\phi_{max}$) has been elegantly described by Rutter et al. [19] in terms of effective mean stress (total mean stress minus melt pressure) and differential stress (Fig. 5b redrawn from [19]).

At the beginning of our experiments the confining pressure is completely transferred to the melt phase and, consequently, the effective pressure is zero. During the elastic loading of the sample in simple shear experiments the differential stress increases while

360 the effective pressure remains constant at zero because the maximum compressive stress
361 is equal to the tensional stress. Under conditions of pure shear during the elastic loading,
362 the effective mean stress increases by one-third relative to the differential stress,
363 following the no-tension line. This line separates the field of entirely compressive stress
364 on the right hand side from the field of differential stress where at least one tensile
365 component is present on the left hand side [19]. The irreversible deformation of the
366 material (yield point, Y or Y^I in Fig. 5b) initiates when the yield surface is encountered.
367 At this point, since all the crystals are in reciprocal contact, a certain amount of dilation
368 has to occur to accommodate the deformation. The dilation induces a decrease of the
369 pore-fluid pressure and, consequently, the effective stress path starts to deviate to the
370 right (Fig. 5b). Differential stress and effective mean stress rise until the critical state line
371 is reached and deformation continues at constant volume, constant differential stress and
372 constant melt pressure (F in Fig. 5b) [19]. From the yielding point (Y or Y^I) to the flow at
373 constant differential stress, the evolution of the microstructures induces a certain amount
374 of strain hardening, as observed in our experiments, both in torsion and compression tests
375 (Fig. 1 and 5b). Due to the shape of the yielding surfaces [19] and to the different loading
376 paths followed by simple and pure shear tests, the total strain required to reach flow is
377 less in compression experiments (Fig. 1 and 5 and Table 1).

378 The dilation that is required to produce flow in the system produces local compaction of
379 the grains [25], which in turn induces a local increase in the melt pressure. These local
380 pressure gradients force the melt to move relative to the crystals toward regions that are
381 under higher effective pressure (lower melt pressure) where the deformation rates are
382 higher [19]. In simple shear experiments the maximum compressive stress is oriented at

383 45° with respect to the shear plane; compaction is expected to occur at high angle with
384 respect to this component and dilation at low angle.

385 This process could well be responsible for the generation of crystal and melt-rich bands
386 observed in our experiments, which we consequently interpret as strain localization
387 features. The angle of the localization bands of ±30 ° reflects minimization of work
388 required to deform the material for such a configuration [25]. Once the melt-enriched
389 bands are established, any further deformation localizes along these zones of weakness
390 (Fig. 5).

391 The amount of dilation required to reach flow at constant differential stress is a function
392 of both, the crystal fraction and the applied strain rate ($F\text{-}F^{I}$ in Fig. 5b). Thus, we infer
393 that in the Newtonian region the melt-pressure gradients (due to local dilation and local
394 compaction) are insufficient to induce significant segregation of melt from crystals. At
395 the onset of shear thinning the strain rate or the stress are high enough to induce the
396 generation of localization bands that facilitate the flow and are responsible for the shear
397 thinning behavior observed in our experiments. Increasing the strain rate increases the
398 melt pressure gradient thereby favoring the segregation of the melt phase from the
399 crystals. This melt-crystal segregation can be envisaged as a reordering of the material,
400 which tends to minimize the energy required for flow. When this reorganization has
401 achieved an optimal configuration, any further increase of strain rate will not lead to an
402 additional decrease of the viscosity; such a micro-structural configuration reflects the
403 attainment and existence of the region of Binghamian behavior at high shear strain rates.

The link between weak, melt-rich zones and the rheological transitions can, in turn, explain the observation that the relative decrease of viscosity due to shear thinning (Log η_r/ Log $\eta_{r(Newtonian)}$) is higher for lower crystal fractions (Fig. 1b). In the case of high solid fractions (ϕ=0.7 and ϕ=0.8), there are insufficient amounts of melt contained in the localization bands to avoid particles interactions, whereas for solid fraction close to the maximum packing (ϕ=0.5 and ϕ=0.6), the segregation of melt from crystals is able to produce localization bands with thicknesses that are sufficient to strongly reduce the contacts between the crystals. The substantial reduction of particle interactions produces, therefore, a higher relative decrease of viscosity, with increasing strain rate, compared to the high solid fraction materials.

5. Rheological Model

In order to implement the complex rheology of crystal-bearing magmas in numerical codes utilized to simulate conduit flow dynamics, the rheological data obtained from the experiments were mathematically treated with a system of equations that account for both, (i) the increase of the η_r with increasing crystal content, and (ii) the decrease of η_r with increasing $\dot{\gamma}$. The effect of temperature on the relative viscosity (η_r) is implicitly included in the definition of η_r, i.e. increasing temperature results in decreasing viscosity of the melt-phase.

The sigmoidal increase of η_r as a function of increasing ϕ is described with a modified version of the semi-empirical Equation (3) given by Costa et al. [37]:

$$\eta_r(\phi) = \frac{1 + \left(\frac{\phi}{\phi_{max}}\right)^{\delta}}{\left(1 - \alpha \mathrm{erf}\left\{\frac{\sqrt{\pi}}{2\alpha}\frac{\phi}{\phi_{max}}\left[1 + \left(\frac{\phi}{\phi_{max}}\right)^{\gamma}\right]\right\}\right)^{B\phi_{max}}} \quad (3)$$

where α, δ, ϕ_{max} (maximum solid packing fraction), and γ are adjustable parameters. B is the Einstein coefficient that was kept constant during the fitting to its theoretical value of 2.5 [38].

A continuous trend of η_{app} as a function of $\dot{\gamma}$ was obtained from our stress – strain-rate data by fitting them with a phenomenological flow law that accounts for the $\dot{\gamma}$-dependent rheology of magmatic suspensions (Eq. 4) as proposed by Brückner et al. [27]:

$$\tau(\dot{\gamma}) = m\eta_{\infty 1}\dot{\gamma} + \tau_0 \cdot \left[1 - \exp\left(-\dot{\gamma}/\dot{\gamma}_{c1}\right)\right] \quad (4)$$

where τ is the shear stress, m is a geometrical factor that is equal to 1 in shear experiments, $\eta_{\infty 1}$ is the limiting viscosity at high $\dot{\gamma}$-values prior to the onset of the visco-elastic behavior of the suspending liquid phase, τ_0 is the fictive yield strength (value of shear stress extrapolated to zero $\dot{\gamma}$), and $\dot{\gamma}_{c1}$ is the critical $\dot{\gamma}$ where the first non-Newtonian transition takes place. Dividing Equation 4 by $\dot{\gamma}$ results the apparent viscosity at each value of $\dot{\gamma}$:

$$\eta_{app}(\dot{\gamma}) = \eta_{\infty 1} + (\tau_0/\dot{\gamma}) \cdot \left[1 - \exp\left(-\dot{\gamma}/\dot{\gamma}_{c1}\right)\right] \quad (5)$$

The numerical results from the fitting procedure using Equation 5 and the parameters $\eta_{\infty 1}$, τ_0 and $\dot{\gamma}_{c1}$, are displayed as solid lines in Figures 3a and 3b.

5.2. A 3D equation for ϕ - $\dot{\gamma}$ dependent viscosity of partially crystallized magmas

444 In order to describe changes in the relative viscosity (η_r) over the entire range of solid
445 fractions between $0<\phi\leq 0.8$ the new experimental data produced in this study were
446 combined with literature data obtained at low degrees of solid fraction ($0<\phi\leq 0.3$) [9].
447 The crystal-induced shear thinning effects for $\phi\leq 0.3$ are very weak (around 0.1-0.2 log
448 units) [26, 29] and, thus, for $0<\phi\leq 0.3$ η_r was assumed to be independent of $\dot{\gamma}$. Using
449 Equation 5, η_r values were computed for strain rates between 10^{-7} to $10^{-0.5}$ s^{-1}. These
450 relative viscosity data were fitted with Equation 3 as a function of ϕ at different values of
451 $\dot{\gamma}$ to constrain the variations of the fitting parameters (α, δ, ϕ_{max}, and γ) with respect to $\dot{\gamma}$
452 (Fig. 2). Variations of the fitting parameters as a function of $\dot{\gamma}$ were then approximated
453 with the following set of equations:

454 $$\phi_{max} = 0.066499 \cdot \tanh(0.913424 \cdot \log10(\dot{\gamma}) + 3.850623) + 0.591806 \quad (6)$$

455 $$\delta = -6.301095 \cdot \tanh(0.818496 \cdot \log10(\dot{\gamma}) + 2.86) + 7.462405 \quad (7)$$

456 $$\alpha = -0.000378 \cdot \tanh(1.148101 \cdot \log_{10}(\dot{\gamma}) + 3.92) + 0.999572 \quad (8)$$

457 $$\gamma = 3.987815 \cdot \tanh(0.8908 \cdot \log10(\dot{\gamma}) + 3.24) + 5.099645 \quad (9)$$

458 Calculated relative viscosities obtained from the model (Equations 3, 6-9) are compared
459 with our experimental data in Figure 2.
460 The combination of Equations (3) with (6), (7), (8), and (9) results in a complete (3D)
461 rheological model describing η_r as a function of both, ϕ and $\dot{\gamma}$ (Fig. 6). Incorporating
462 rheological models that describe the viscosity of the suspending liquid phase (e.g. [14,
463 15] furthermore allows the prediction of the temperature and strain rate dependence of
464 the apparent magma viscosity. This, in turn, can be used to calculate the dependence of

the fictive yield strength (τ_0) on crystal fraction and temperature by fitting the apparent viscosity of the magma as a function of strain rate to Equation (5).

It is important to note that our experiments only approached the Binghamian field, therefore, an additional decrease of the viscosity could occur when the strain rate is increased to values higher than 10^{-3} s^{-1} (maximum value reached in our experiments). Furthermore, viscous heating effect could start to play an important role for such high strain rate values and this phenomenon would further decrease the viscosity. These observations imply that for strain rates higher then 10^{-3} s^{-1} our equation only provides an upper limit of viscosity.

The errors of the predicted η_r values as a function of ϕ and $\dot{\gamma}$ were evaluated by using two different models to estimate the viscosity of the pure melt phase [14, 15] and by performing experiments at different temperatures but identical crystal fraction, where the only difference was the viscosity of the melt phase. The error on the η_r calculation due to experimental uncertainty, the viscosity of the suspending melt phase, and the fitting procedure amounts to a maximum value of 0.3 log units as illustrated in Figure 2 by the differences between the experimental values and the curves obtained from the model (Eq. 3, 6-9).

6. Numerical modeling

6.1. Physical modeling of magma flow

The parameterization for non-Newtonian viscosity of crystal-bearing magmas expressed by Equations 5-8 was introduced into the numerical code utilized to model multiphase magma ascent [10]. The model describes the 1D, steady, isothermal, separated flow of

488 multiphase magma along a cylindrical volcanic conduit. The flowing magma is described
489 as a homogeneous mixture of liquid and solid phases, mechanically interacting with a gas
490 phase. The gas phase is contained in the form of bubbles below the fragmentation level
491 and it is modeled as a continuous phase with dispersed pyroclasts above this level.
492 The properties of magma depend on the local pressure-composition conditions. Volatile
493 saturation is determined by modeling the non-ideal gas-liquid thermodynamic
494 equilibrium [4]. Liquid-crystal density is computed with the model given by Lange [39]
495 and standard mixing rules were applied (as reported in [12]). Gas density is calculated
496 through the Modified Redlich-Kwong equation provided by Kerrick et al. [40].
497 The friction terms in the momentum equations require a description of mixture viscosity.
498 This in turn depends on the flow regime (either bubbly flow below magma fragmentation,
499 or gas-particle flow above it), on the viscosity of the continuous phase (liquid magma
500 below fragmentation, gas above it), and on the volume fraction of the dispersed phases
501 (crystals and gas bubbles below fragmentation, pyroclasts above it). Liquid viscosity is
502 modeled through semi-empirical TVF-like equation [14, 41]. Gas bubbles, assumed for
503 simplicity to be undeformable, are accounted for as described in [10]. The effects of
504 crystals on the rheology are taken into account by either using the new parameterization
505 presented here (Eqs. 3, 6-9) that includes the effects of non-Newtonian $\dot{\gamma}$ –induced
506 decrease in η_{app}, or the simpler Newtonian model proposed by Costa et al. [37].
507
508 *6.2 Numerical simulations*
509 The numerical simulations were conducted to evaluate the effects of non-Newtonian
510 behavior of crystal-bearing magmas on the dynamics of magma ascent and fragmentation

511 along volcanic conduits during explosive eruptions. In order to assess the role of high
512 crystal contents and $\dot{\gamma}$ -induced decrease of η_{app} of the liquid + crystal homogeneous
513 mixture, we conducted parametric simulations by comparing the results obtained with the
514 present model of suspension rheology with those obtained with the Newtonian model
515 given in [37] for crystal-bearing magmas. In order to evaluate the results over a wide
516 spectrum of conditions, we repeated the simulations by determining the occurrence of
517 magma fragmentation by either the visco-elastic criterion in [8] or the gas bubble
518 overpressure criterion in [7], and by using two different magmas of rhyolitic and trachytic
519 composition, each with a corresponding typical eruptive temperature. For each set of
520 conditions, the crystal fraction of the erupted magma were let to vary from zero up to
521 ϕ=0.55 (relative to the degassed magma). These crystal fractions represent the most
522 interesting range of crystallinity at which the most explosive eruptions occur [e.g. 11-13].
523 Moreover, as the experiments demonstrate, already for ϕ=0.5 the non-Newtonian
524 character of magma starts to exert a strong control on the magma viscosity. The highest
525 crystal contents reflect conditions over which numerical convergence is not achieved, due
526 to very high mixture viscosity hence very large gradients of flow variables along the
527 volcanic conduit [8].
528
529 6.3 *Results of numerical simulations*
530 The numerical results illustrate the effects of incorporating non-Newtonian rheology of
531 crystal-bearing magmas in magma ascent modeling on the dynamics of magma ascent
532 and on the occurrence of magma fragmentation. In addition, these models show the
533 different dynamics associated with the discharge of magmas having different crystal

534 contents. Differences in the calculated magma flow dynamics due to different
535 composition of the liquid magma are not discussed here, since they are the subject of
536 previous work [42, 43].
537 Figure 7 shows the calculated distribution of the mixture viscosity and of η_r along the
538 volcanic conduit for conditions pertaining to trachytic magma; the visco-elastic
539 fragmentation criterion of Papale [8] has been adopted, and two crystal fractions, ϕ=0.25
540 and ϕ=0.55, were considered. In both cases, non-Newtonian rheology results in a
541 shallower magma fragmentation level. With ϕ=0.25 (Fig. 7a), the rise of the
542 fragmentation level is only about 250 m and fragmentation occurs for a η_r more than 1
543 order of magnitude lower than for the case where Newtonian behavior is assumed. With
544 ϕ=0.55 (Fig. 7b), the uplift of the fragmentation level becomes as large as 2360 m. In this
545 case, the η_r strongly decreases due to non-Newtonian rheology. Contrarily, with
546 Newtonian rheology, the η_r increases approaching fragmentation, reflecting an increase
547 of crystal volume fraction due to density increase of the liquid phase upon degassing. At
548 the level where fragmentation occurs the η_r determined with non-Newtonian rheology is
549 about 2 orders of magnitude lower than for Newtonian rheology.
550 In spite of the contrasting trends in η_r, the viscosity of the multiphase magma always
551 increases below fragmentation, mainly due to the large effect of H_2O exsolution from the
552 liquid on viscosity [14, 15, 41]. Above the magma fragmentation level, the mixture
553 viscosity suddenly decreases by many orders of magnitude approaching that of the
554 continuous gas phase. This is a consequence of the fundamental change in the continuum
555 properties of the magmatic mixture upon fragmentation.

Figure 8 shows the calculated mass flow-rate and pressure at the conduit exit level obtained for the simulations pertaining to the trachytic magma, the fragmentation criterion as given by Papale [8], and crystal fractions varying from ϕ=0 to ϕ=0.55. The numerical results indicate that over the range of crystal contents considered, the mass flow rate decreases by a factor of 6-10 and the exit pressure decreases by about a factor of 10. Non-Newtonian effects tend to reduce mass flow-rates and pressure decreases; these effects vanish when zero crystal content is approached. However, in spite of the large variations in the distribution of magma viscosity (and other flow variables such as gas volume fraction and phase velocities and densities) inside the volcanic conduit in Figure 7, these quantities change only a small fraction even at large crystal content. Other flow variables (not reported in the Figure) show similar small variations when comparing their values at the conduit exit obtained by either Newtonian or non-Newtonian rheology of the crystal-bearing magma.

Figure 9 summarizes the conditions calculated at magma fragmentation in terms of depth and magma vesicularity for all simulations performed. In all cases, increasing crystal contents in the discharged magma result in a deepening of the fragmentation level and in a decrease of magma vesicularity at fragmentation. The use of non-Newtonian rheology strongly restricts the range of such variations. As an example, fragmentation depth and magma vesicularity at fragmentation computed for Newtonian rheology and the fragmentation criterion given by Melnik [7] amounts to about 6.6 km and 20 vol. % for a trachytic magma. The same quantities become 3.6 km and 50 vol. % when using non-Newtonian rheology. It is remarkable that the overall vesicularity range covered by all the simulations performed with the two fragmentation criteria is largely reduced by the use of

579 non-Newtonian rheology: The total range is <5– 90 vol.% with Newtonian rheology and
580 reduced to 40 – 90 vol.% with non-Newtonian rheology.
581
582 **7. Conclusions**
583 The experiments reported here demonstrate that the introduction of suspended crystals in
584 a melt phase produces an increase in the relative viscosity η_r and enhances $\dot{\gamma}$-dependent
585 rheology. The shear thinning behavior observed in our experiments is caused by a
586 geometrical redistribution of suspended particles and melt that facilitate the flow of
587 magma resulting in a reduction of viscosity with increasing $\dot{\gamma}$. The generation of melt-
588 enriched bands requires additional, more detailed investigation because these processes
589 could exert strong controls on processes such as the distribution of gas bubble upon
590 volatile exsolution. The coincidence between the maximum applied stress and the
591 direction of the flow parallel to the walls in volcanic conduits is optimal to produce melt
592 enriched bands parallel to the flow direction. The alignment of bubbles parallel to the
593 direction of the flow could, in turn, result in a strong effect on magma permeability and
594 consequent exsolution of volatiles during rise from the magma chamber.
595 The system of Equations (3, 6-9) presented in this contribution successfully describes the
596 complex rheological behavior of crystal-bearing magmas. These equations provide the
597 basis to evaluate the effects of micro-scale deformation processes occurring during
598 magma flow on the macroscopic behavior of magmas rising inside volcanic conduits
599 during explosive eruptions. The numerical simulations of magma ascent and
600 fragmentation along volcanic conduits infer that the introduction of non-Newtonian
601 rheology of crystal-bearing magma results in large variations in the fragmentation

602 conditions and distribution of flow variables along the conduit. However, the restricted
603 variation of the calculated mass flow-rate and conduit exit conditions do not reflect the
604 large changes observed within the conduit. This is most probably related to the counter-
605 acting effects of reduced η_{app} and increased length of the highly viscous region below
606 fragmentation [43] resulting from the introduction of non-Newtonian rheology. In
607 conclusion, the present results suggest that non-Newtonian behavior significantly affects
608 the internal conduit dynamics and the physical characteristics of magmas at the
609 fragmentation level, while the general eruption dynamics are more sensitive to
610 Newtonian viscosity of the liquid fraction. The introduction of non-Newtonian rheology
611 has the effect of largely decreasing the extent to which crystals, and in general solid
612 particles transported in the magma (e.g. xenoliths or lithics), affect the fragmentation
613 conditions, although the general trend due to increasing amount of crystals does not
614 change. The crystal content of the erupted magma, which resulted to be the magma
615 characteristic that most significantly decreased the vesicularity of the magma at
616 fragmentation, now turns to be much less effective when taking into account non-
617 Newtonian rheology.
618 Finally, it must be stressed that the present simulations are performed under the
619 simplifying assumption of 1D magma flow. It is likely that other complexities due to
620 non-Newtonian rheology may arise when considering multi-D phenomena. As an
621 example, it may be expected that non-Newtonian rheology plays a significant role in
622 decreasing the local η_{app} close to conduit walls where shear stress concentrates. In such a
623 case, the process of viscous dissipation and local increase of temperature [44-46] would

become important, requiring specific numerical simulations to be performed to evaluate these additional effects.

8. Acknowledgements

This research was supported by the Swiss National Science Foundation (grants 200021-103845 and 200020-111852). We wish to thank Paola Ardia for supplying the glass starting material used in the experiments and for the valuable discussions. The experimental part of this work would not have been possible without the analytical support of the microprobe laboratory and all the technicians of the workshop at the Department of Earth Sciences at ETH Zurich. We particularly acknowledge Robert Hofmann for the great capability of making everything possible. We gratefully acknowledge Claude Jaupart for the professional handling of the manuscript, and Martin O. Saar and two anonymous reviewers for their thoughtful comments that greatly improved the manuscript.

638 **References**

639 [1] D.B. Dingwell, Volcanic Dilemma: flow or blow? Science 273 (1996) 1054-1055.

640 [2] E.W. Llewellin, A. Manga, Bubble suspension rheology and implications for
641 conduit flow, J. Volcanol. Geotherm. Res. 143 (1-3) (2005) 205-217.

642 [3] A.M. Lejeune, Y. Bottiga, T.W. Trull, P. Richet, Rheology of bubble-bearing
643 magmas, Earth Planet. Sci. Lett. 166 (1998) 71-84.

644 [4] P. Papale, R. Moretti, D. Barbato, The compositional dependence of the
645 saturation surface of H_2O+CO_2 fluids in silicate melts, Chem. Geol. 229 (2006)
646 78-95.

647 [5] S.L. Webb, D.B. Dingwell, Non-Newtonian rheology of igneous melts at high
648 stresses and strain rate: experimental results for rhyolite, andesite, basalt, and
649 nephelinite, J. Geophys. Res. 95 (1990) 15695-15701.

650 [6] O. Melnik, R.S.J. Sparks, Nonlinear dynamics of lava dome extrusion, Nature 402
651 (1999) 37-41.

652 [7] O. Melnik, Dynamics of two-phase conduit flow of high-viscosity gas-saturated
653 magma: large variations of sustained explosive eruption intensity, Bull. Volcanol.
654 62 (2000) 153-170.

655 [8] P. Papale, Strain-induced magma fragmentation in explosive eruptions, Nature
656 397 (1999) 425-428.

657 [9] D.G. Thomas, Transport characteristics of suspension .8. A note on viscosity of
658 Newtonian suspensions of uniform spherical particles, J. Colloid Sci. 20 (1965)
659 267-277.

660 [10] P. Papale, Dynamics of magma flow in volcanic conduits with variable
661 fragmentation efficiency and nonequilibrium pumice degassing, J. Geophys. Res.
662 (2001)106 11043-11065.
663 [11] O. Bachmann, M.A. Dungan, P.W. Lipman, The Fish Canyon magma body, San
664 Juan volcanic field, Colorado: rejuvenation and eruption of an upper-crustal
665 batholith, J.Petrol. 43 (2002) 1469-1503.
666 [12] M. Rosi, C. Principe, R. Vecci, The 1631 Vesuvius Eruption - A Reconstruction
667 Based On Historical And Stratigraphical Data J. Volcanol. Geotherm. Res. 58
668 (1993) 151-182.
669 [13] M.J. Rutherford, L. Baker, J.S. Pallister, Experimental petrology applied to
670 volcanic processes, Eos (1993) 74 671.
671 [14] K.U. Hess, D.B. Dingwell, Viscosities of hydrous leucogranitic melts: A non-
672 Arrhenian model, Am. Mineral. 81 (1996) 1297-1300.
673 [15] D. Giordano, J.K. Russel, D.B. Dingwell, Viscosity of magmatic liquids: a model
674 for volcanology. Geophysical research abstract 9 (2007).
675 [16] M.S. Paterson, D.L. Olgaard, Rock deformation tests to large shear strains in
676 torsion, J. Structural Geology 22 (2000) 1341-1358.
677 [17] A. Barnhoorn, M. Bystricky, L. Burlini, K. Kunze, The role of recrystallization on
678 the deformation behaviour of calcite rocks: large strain in torsion experiments on
679 Carrara marble, J. Structural Geology 36 (2004) 885-903.
680 [18] H.J. Frost and M.F. Ashby, Deformation-Mechanism Maps, (1982) pp. 11-17.

[19] E.H. Rutter, K.H. Brodie, D.H. Irving, Flow of synthetic, wet, partially molten "granite" under undrained conditions: an experimental study, J. Geophys. Res. 111 (2006) doi:10.1029/2005JB004257.

[20] G.I. Krieger, Rheology of monodispersed lattices, Adv. Colloid Interface Sci. 3 (1972) 111-136.

[21] J.S. Chong, E.B. Christiansen, A.D. Baer, Rheology of concentrated suspensions, J. Appl. Polym. Sci. 15 (1971) 2007-2021.

[22] M.O. Saar, M. Manga, K.V. Cashman, S. Fremouw, Numerical models of the onset of yield strength in crystal-melt suspensions, Earth Planet. Sci. Lett. 187 (2001) 367-379.

[23] E. J. Garboczi, K.A. Snyder, J.F. Douglas, Geometrical percolation threshold of overlapping ellipsoids. Phys. Rev. 52 (1995) 819-828.

[24] K.M. Kulkarni, S. Kalpakjian, A study of barreling as an example of free deformation in plastic working, J. Eng. Ind. 91 (1969) 743-754.

[25] B.K. Holtzman, D.L. Kohlstedt, J.P. Morgan, Viscous energy dissipation and strain partitioning in partially molten rocks, J. Petrol. 46 (2005) 2569-2592.

[26] F.J. Ryerson, H.C. Weed, A.J. Piwinskii, Rheology of subliquidus magmas .1. picritic compositions, J. Geophys. Res. 93 (1988) 3421-3436.

[27] R. Brückner, J. Deubener, Description and interpretation of the two phase flow behavior of melts with suspended crystals, J. Non-Cryst. Solids 209 (1997) 283-291.

[28] J. Deubener, R. Bruckner, Influence of nucleation and crystallization on the rheological properties of lithium disilicate melt, J. Non-Cryst. Solids 209 (1997) 96-111.

[29] H. Sato, Viscosity measurement of subliquidus magmas: 1707 basalt of Fuji volcano, Journal of Mineralogical and Petrological Sciences 100 (2005) 133-142.

[30] T. Scott, D.L. Kohlstedt, The effect of large melt fraction on the deformation behavior of peridotite, Earth Planet. Sci. Lett. 246 177-187 (2006).

[31] C.G. Dekruif, E.M.F. Vanlersel, A. Vrij, W.B. Russel, Hard-sphere colloidal dispersions- viscosity as function of shear rate and volume fraction, J. Chem. Phys. 83 (1985) 4717-4725.

[32] J.C. Vanderwerff, C.G. Dekruif, Hard-sphere colloidal dispersions- the scaling of rheological properties with particles-size, volume fraction, and shear rate, J. Rheol. 33 (1989) 421-454.

[33] R. Eriksson, M. Hayashi, S. Seetharaman, Thermal diffusivity measurements of liquid silicate melts, Int. J. Thermophysics, 24 (2003) 785-796.

[34] C.L. Rosemberg, M.R. Handy, Experimental deformation of partially melted granite revisited: implications for the continental crust, J. Metamorphic Geology 23 (2005) 19-28.

[35] W.E. Smith, C.F. Zukoski, Flow properties of hard structured particle suspensions, J. Rheol. 48 (2004) 1375-1388.

[36] M.K. Lyon, Structure formation in moderately concentrated viscoelastic suspensions in simple shear flow, J. Rheol. 45 (2001) 881-890.

724 [37] A. Costa, O. Melnik, R. S. J. Sparks, B. Voight, Control of magma flow in dykes
725 on cyclic lava dome extrusion, Geophys. Res. Lett. 34 (2007) doi:
726 10.1029/2006GL027466.
727 [38] A. Einstein, Eine neue Bestimmung der Moleküldimensionen, Annalen der
728 Physik 19 (1906) 289-306.
729 [39] R.A. Lange, The effect of H_2O, CO_2 and F on the density and viscosity of silicate
730 melts, In: MR Carroll, JR Holloway (eds) Volatiles in magmas (Reviews in
731 mineralogy, 30) Mineral. Soc. Am., Washington DC (1994), pp 331-369.
732 [40] D.M. Kerrick, G.K. Jacobs, A modified Redlich-Kwong equation for H_2O, CO_2,
733 and H_2O-CO_2 mixtures at elevated pressures and temperatures, Am. J. Sci. 281
734 (1981) 735-767.
735 [41] C. Romano, D. Giordano, P. Papale, V. Mincione, D.B. Dingwell, M. Rosi, The
736 dry and hydrous viscosities of silicate melts from Vesuvius and Phlegrean Fields,
737 Chem. Geol., 202 (2003), 23-38.
738 [42] P. Papale, A. Neri, G. Macedonio, The role of magma composition and water
739 content in explosive eruptions: 1. Conduit ascent dynamics, J. Volcanol.
740 Geotherm. Res., 87 (1998), 75-93.
741 [43] M. Polacci, P. Papale, D. Del Seppia, D. Giordano, C. Romano, Dynamics of
742 magma ascent and fragmentation in trachytic versus rhyolitic eruptions, J.
743 Volcanol. Geotherm. Res., 131 (2004), 93-108.
744 [44] A. Costa, G. Macedonio, Viscous heating in fluids with temperature-dependent
745 viscosity: implications for magma flows, Nonli. Processes Gephys., 10 (2003),
746 545-555.

747 [45] A. Costa, G. Macedonio, Viscous heating effects in fluids with temperature-
748 dependent viscosity: triggering of secondary flows, J. Fluid Mechanics, 540
749 (2005), doi: 10.1017/S0022112005006075.
750 [46] E.A. Vedeneeva, O. Melnik, A.A. Barmin, and R.S.J. Sparks, Viscous dissipation
751 in explosive volcanic flows, Geophys. Res. Lett., 32 (2005), doi:
752 10.1029/2004GL020954.

753 **Figure Captions**

754 **Figure 1**: Selected examples of experiments performed in torsion and compression
755 configuration at 250 MPa confining pressure. The relevant conditions for each
756 experiment (crystal fraction (ϕ), temperature and strain rates ($\dot{\gamma}$) in s^{-1} are indicated as
757 labels attached to each curve. a) Recorded stress values plotted against strain. The steps
758 in the individual curves represent the increase of stress due to an increase of strain rate
759 during the experiments (i.e. strain rate stepping experiments, for details see text). The
760 Inset illustrates the fitting procedure performed to obtain the apparent viscosity with
761 respect to the strain rate applying Equation 4. The data represent the maximum stress
762 reached during the flow of the material for each strain rate. The stress values tend to
763 decrease to zero at zero strain rate testifying the absence of yield strength. The"fictive
764 yield strength" (τ_0, Table 1; see text for more details) is obtained by extrapolation of the
765 stress values at relatively high strain rate ($>10^{-4}$ s^{-1}) to zero strain rate (dashed line). b)
766 Calculated apparent viscosities obtained from individual strain rates ($\eta_{app}=\tau/\dot{\gamma}$) plotted
767 versus strain. Increasing the strain rate for any given crystal fraction (ϕ) and temperature
768 induces a decrease of viscosity interpreted as shear thinning behavior.

769

770 **Figure 2**: Logarithmic values of relative viscosity (η_r) as a function of solid fraction (ϕ).
771 Symbols represent experimental data from this study except the black crosses that are
772 data taken from literature [9]. The average error in relative viscosity indicated by a bar
773 on the diagram represents the uncertainty of the calculated viscosities based on repeat
774 experiments performed with the same crystal fractions at different temperature and
775 considering the differences in the calculated viscosities of the suspending liquids using

776 the algorithms provided by [14] and [15]. Continuous lines represent calculated η_r
777 obtained from Equations 3, 6-9 and a viscosity of the suspending melt melt phase
778 calculated with algorithm provided by [14]. The relative viscosities (η_r) increases non-
779 linearly with increasing suspended solid fraction. ϕ_{max} corresponds to the onset of the
780 exponential increase of η_r and increases with increasing $\dot{\gamma}$ as indicated by the vertical,
781 broken lines for low and high strain rates respectively.
782
783 **Figure 3**: a) Logarithmic values of relative viscosity (η_r) plotted as a function of the
784 logarithm of the strain-rate ($\dot{\gamma}$, s^{-1}). This diagram illustrates the dependence of η_r on solid
785 fraction and highlights the shear thinning behavior of crystal bearing samples with
786 increasing $\dot{\gamma}$. b) Variation of the logarithmic values of the relative viscosity at a given
787 strain-rate divided by the relative viscosity in the Newtonian region
788 ($Log\eta_r/Log\eta r_{(Newtonian)}$, i.e. at very low strain-rates) as a function of the logarithm of the
789 strain rate. Details of the experiments are provided in Tables 1.
790
791 **Figure 4**: Back scattered electron (BSE) images of recovered, deformed samples. The
792 glass phase is light grey and the quartz particles are dark grey. For each individual image,
793 a scale bar, the crystal fraction (ϕ), the experimental temperature, a sketch of the
794 orientation of the applied stress field, and the total applied strain are indicated in the
795 lower left corner. The white bars drawn in the sketched samples indicate the portions of
796 the samples where the images were taken. The arrows in the BSE images indicate the
797 strain localization bands. The localization bands are oriented at around 30 and 150° with

798 respect to the direction of flow in all samples regardless of the solid fraction and total
799 applied strain.
800
801 **Figure 5:** Diagram illustrating the relationships between observed rheological behavior
802 and microstructures. a) Apparent viscosity plotted against strain. The strain rate increases
803 from the left to the right. In the low strain rate region (left panel) the viscosity does not
804 vary with strain rate corresponding to Newtonian behavior (i.e. viscosity is independent
805 of strain rate). Increase of strain rate first leads to a region of non-Newtonian and
806 ultimately Binghamian behavior (for detailed explanations see text). The pictures inserted
807 in the lower part of the diagram visualize the microstructures generated during the
808 experiments that are responsible for the observed rheological transitions. b) Rheological
809 behavior of crystal bearing magmas in torsion and compression experiments interpreted
810 in terms of differential stress and effective mean stress; Figure redrawn from [19]. The
811 paths OY and OY^I represent the loading trajectories for torsion and compression
812 experiments, respectively. At Y or Y^I, depending on the imposed stress field (simple
813 shear or pure shear), the loading path intersects the yielding surface where irreversible
814 deformation of the sample starts. The deformation induces dilation that decreases the
815 melt pressure thereby driving the loading path to the right toward the critical state line. In
816 F, the flow of the material continues at constant differential stress and constant effective
817 mean stress. Increasing crystal fractions or applied strain rates expand the yielding
818 surface; i.e. for material with constant crystal fraction and constant temperature, an
819 increase of strain rate shifts the onset of flow from F to F^I (for more detail see [19]). The
820 amount of dilation is inversely proportional to the melt pressure and directly proportional

821 to strain rate. Consequently, with increasing strain rate, dilation increases concomitantly
822 with the difference in melt pressure between the yielding point (Y, Y') and the flow (F,
823 F'). The increase of dilation with strain rate promotes the localization features observed
824 in our microstructures, which are responsible for the transition from Newtonian to non-
825 Newtonian behavior. The microstructures corresponding to different rheological
826 behaviors (Newtonian at low strain rates and non-Newtonian at high strain rates) are
827 sketched as inserts on the right hand side of the Figure.
828
829 **Figure 6**: Variation diagram showing the logarithm of the relative viscosity ($\log \eta_r$) as a
830 function of crystal fraction (ϕ) and the logarithm of the strain-rate ($\log \dot{\gamma}$) (s^{-1}). The η_r
831 values are calculated using Equations (3), and (6-9). The viscosity of the pure melt phase
832 is computed from the equation reported in [14]. The heavy line on the right side depicts
833 the projection of the $\log \eta_r$ at a strain-rate corresponding to10^{-7} s^{-1} and highlights the
834 influence of $\dot{\gamma}$ on the maximum packing fraction and the shear thinning behavior of
835 crystal bearing magmas.
836
837 **Figure 7**: Diagrams illustrating the results of numerical modeling of volcanic conduit
838 dynamics: Computed variations of the logarithm of the viscosity of the mixture ($\log \eta_{mix}$,
839 left side) and the logarithm of the relative viscosity ($\log \eta_r$, right side) as a function of
840 depth below the surface for two crystal fractions, a) ϕ=0.25 and b) ϕ=0.55, for a trachytic
841 magma (composition given in [41]) with a temperature of 947 °C. The solid and dashed
842 lines refer to the crystal-melt non-Newtonian rheological model presented in this paper
843 and to the Newtonian model given in [37], respectively. Calculations reported in this

Figure and in Figures 8 and 9 have been conducted with a conduit length and diameter of 8000 and 50 m, respectively, a stagnation pressure of 200 MPa, 6 wt. % water content (= H_2O-content of the melt phase) and crystal fractions relative to the degassed magma ranging from ϕ=0 to ϕ=0.55. Further details of the dynamic conduit model are given in [10].

Figure 8: Diagram illustrating the calculated mass flow rate a) and conduit exit pressure b) as a function of variable crystal fractions of the erupted magma for a trachytic magma (composition given in [41]) with a temperature of 947 °C. The solid lines and circles, and the dashed lines and stars, refer to the crystal-melt systems employing the non-Newtonian rheological model reported in this paper and to the Newtonian model given in [37], respectively.

Figure 9: Diagram illustrating the calculated fragmentation conditions, in terms of depth and magma vesicularity (volume of gas) for a) rhyolitic (reported in [43], temperature of 827 °C); and b) trachytic magma compositions (reported in [41], temperature of 947 °C) for different crystal fractions (= numbers close to the symbols), and different fragmentation criteria according to [7] and [8]. The solid lines and circles, and the dashed lines and stars, refer to the crystal-melt systems employing the non-Newtonian rheological model reported in this paper and to the Newtonian model given in [37], respectively.

Table 1: Summary of results of deformation experiments at 250 MPa confining pressure.

867 The data presented in italics are values converted from compression experiments
868 according to equations (38-42) [16]; τ_0 is the fictive yield strength obtained by
869 extrapolating the stress - strain rate curves at high shear strain rate to zero strain rate; the
870 maximum strain attained in these experiments (gamma) is the shear strain rate calculated
871 in torsion multiplied by the duration of the experiment in seconds. Abbreviations: n =
872 stress exponent; gamma = maximum strain; log ηapp = logarithm of the apparent
873 viscosity; log ηr = logarithm of the relative viscosity; log ηr/ log ηr(Newtonian) = the
874 ratio of the logarithms of the relative viscosity at a given strain rate divided by the
875 logarithm of the relative viscosity in the Newtonian field, i.e. at very low strain rate. The
876 definitions of the apparent and relative viscosities are given in the text.
877
878 **Figure 1 on line material**: Logarithmic diagram of torque (Nm) versus strain rate (s^{-1})
879 used to constrain the stress exponent (n) that was utilized to convert torque values into
880 stress values. The thick continuous lines represent the trends of torque-strain rate for
881 material with the stress exponent reported close to the lines. The thin dashed lines are
882 parallel to the thick line and highlight the relationship between the experimental data and
883 derived exponent n for samples with $\phi = 0.5$ at 500°C and $\phi = 0.6$ at 600°C respectively.
884
885 **Table 1 on line material**: Representative electron microprobe analyses of synthetic
886 glasses before and after the deformation experiments
887 The labels for individual experiments (e.g. PO663) refer to Table 1. Standard deviations
888 are 1σ errors.
889

Table 1: Summary of results of deformation experiments at 250 MPa confining pressure.

Exp. N°	n	Gamma	Torque (Nm)	Shear stress (MPa)	Shear strain rate ($s.^{-1}$)	Log η_{app} (Pa·s)	Log η_r (Pa·s)	Logη_r / Log$\eta_{r(Newtonian)}$
ϕ= 0.5 T= 500 °C t_0=90.6 MPa								
PO770	1	0.036	7.1	36.45	3.12E-06	13.07	2.60	0.92
PO770	1	0.049	12.2	62.40	6.12E-06	13.01	2.59	0.92
PO751	1	0.152	15.6	79.61	4.92E-06	13.21	2.63	0.98
PO751	1	0.167	17.3	87.98	7.79E-06	13.05	2.47	0.92
PO751	1	0.144	18.6	94.63	1.14E-05	12.92	2.34	0.87
PO751	2	0.139	23.6	100.19	2.07E-05	12.68	2.10	0.78
PO751	2	0.221	25.5	108.36	2.71E-05	12.60	2.02	0.75
PO751	2	0.425	32.8	139.36	6.21E-05	12.35	1.77	0.66
ϕ= 0.6 T= 600 °C t_0=20.9 MPa								
PO674	1	0.010	1.7	5.01	4.76E-06	12.02	3.50	0.91
PO674	1	0.023	3.2	9.39	8.97E-06	12.02	3.50	0.91
PO674	2	0.055	5.0	14.82	3.09E-05	11.68	3.08	0.80
PO674	2	0.068	6.0	17.58	6.28E-05	11.45	2.85	0.74
PO674	2	0.011	6.9	20.38	9.43E-05	11.33	2.74	0.71
PO674	2	0.163	6.5	19.08	9.14E-05	11.32	2.72	0.71
PO674 c	*4*	*0.167*	*"*	*27.54*	*4.25E-04*	*10.81*	*2.29*	*0.60*
PO674 c	*4*	*0.335*	*"*	*38.46*	*8.84E-04*	*10.64*	*2.12*	*0.55*
ϕ= 0.7 T= 800 °C t_0 = 86.9 MPa								
PO670	1	0.021	5.0	14.61	5.12E-06	12.46	6.59	1.04
PO670	1	0.037	7.9	23.32	8.68E-06	12.43	6.57	1.04
PO670	3	0.101	15.5	38.08	2.52E-05	12.18	6.32	1.00
PO670	3	0.148	20.8	50.98	4.64E-05	12.04	6.18	0.97
PO670	3	0.190	22.6	55.89	5.25E-05	12.03	6.16	0.97
PO670 c	*4*	*0.162*	*"*	*84.62*	*1.25E-04*	*11.83*	*5.97*	*0.94*
PO670 c	*4*	*0.243*	*"*	*108.71*	*3.24E-04*	*11.53*	*5.66*	*0.89*
PO670 c	*4*	*0.399*	*"*	*117.18*	*6.77E-04*	*11.24*	*5.38*	*0.85*
ϕ= 0.7 T= 850 °C t_0 = 38.4 MPa								
PO669	1	0.021	4.2	12.45	5.01E-06	12.40	7.01	0.99
PO669	1	0.064	9.2	27.08	9.19E-06	12.47	7.09	1.00
PO669	3	0.145	13.6	33.46	2.98E-05	12.05	6.67	0.94
PO669	3	0.187	15.6	38.24	6.06E-05	11.80	6.42	0.90
PO669	3	0.238	16.9	41.50	9.33E-05	11.65	6.27	0.88
PO669 c	*4*	*0.080*	*"*	*39.50*	*6.03E-05*	*11.82*	*6.43*	*0.91*
PO669 c	*4*	*0.093*	*"*	*48.48*	*1.65E-04*	*11.47*	*6.09*	*0.86*
PO669 c	*4*	*0.119*	*"*	*54.17*	*4.44E-04*	*11.09*	*5.70*	*0.80*
ϕ= 0.8 T= 850 °C t_0 = 110.7 MPa								
PO673	3	0.047	20.7	86.69	5.55E-06	13.19	7.81	0.97
PO663	3	0.065	24.5	105.37	8.25E-06	13.11	7.72	0.96
PO673	4	0.057	23.9	100.10	9.21E-06	13.04	7.65	0.95
PO673	4	0.080	26.9	112.66	3.17E-05	12.55	7.15	0.89
PO673	4	0.095	28.8	120.53	6.40E-05	12.27	6.87	0.85
PO673 c	*4*	*0.208*	*"*	*120.16*	*1.11E-04*	*12.03*	*6.65*	*0.82*
PO673 c	*4*	*0.212*	*"*	*123.83*	*1.76E-04*	*11.85*	*6.47*	*0.80*
PO673 c	*4*	*0.222*	*"*	*135.82*	*4.70E-04*	*11.46*	*6.08*	*0.75*
ϕ= 0.8 T= 900 °C t_0 = 79.7 MPa								

PO672	3	0.112	18.2	78.18	8.82E-06	12.95	7.91	0.89
PO660	3	0.230	19.1	82.09	2.59E-05	12.50	7.54	0.85
PO660	3	0.263	22.6	96.94	5.27E-05	12.26	7.30	0.82
PO660	3	0.281	23.6	101.52	7.94E-05	12.11	7.15	0.80
PO660 c	*4*	*0.503*	*"*	*104.01*	*1.35E-04*	*11.89*	*6.93*	*0.78*

The data presented in italics are values converted from compression experiments according to equations (38-42) [16]; t_0 is the fictive yield strength obtained by extrapolating the stress - strain rate curves at high shear strain rate to zero strain rate; the maximum strain attained in these experiments (gamma) is the shear strain rate calculated in torsion multiplied by the duration of the experiment in seconds. Abbreviations: n = stress exponent; gamma = maximum strain; log app = logarithm of the apparent viscosity; log r = logarithm of the relative viscosity; log r/ log r(Newtonian) = the ratio of the logarithms of the relative viscosity at a given strain rate divided by the logarithm of the relative viscosity in the Newtonian field, i.e. at very low strain rate. The definitions of the apparent and relative viscosities are given in the text.

906

907

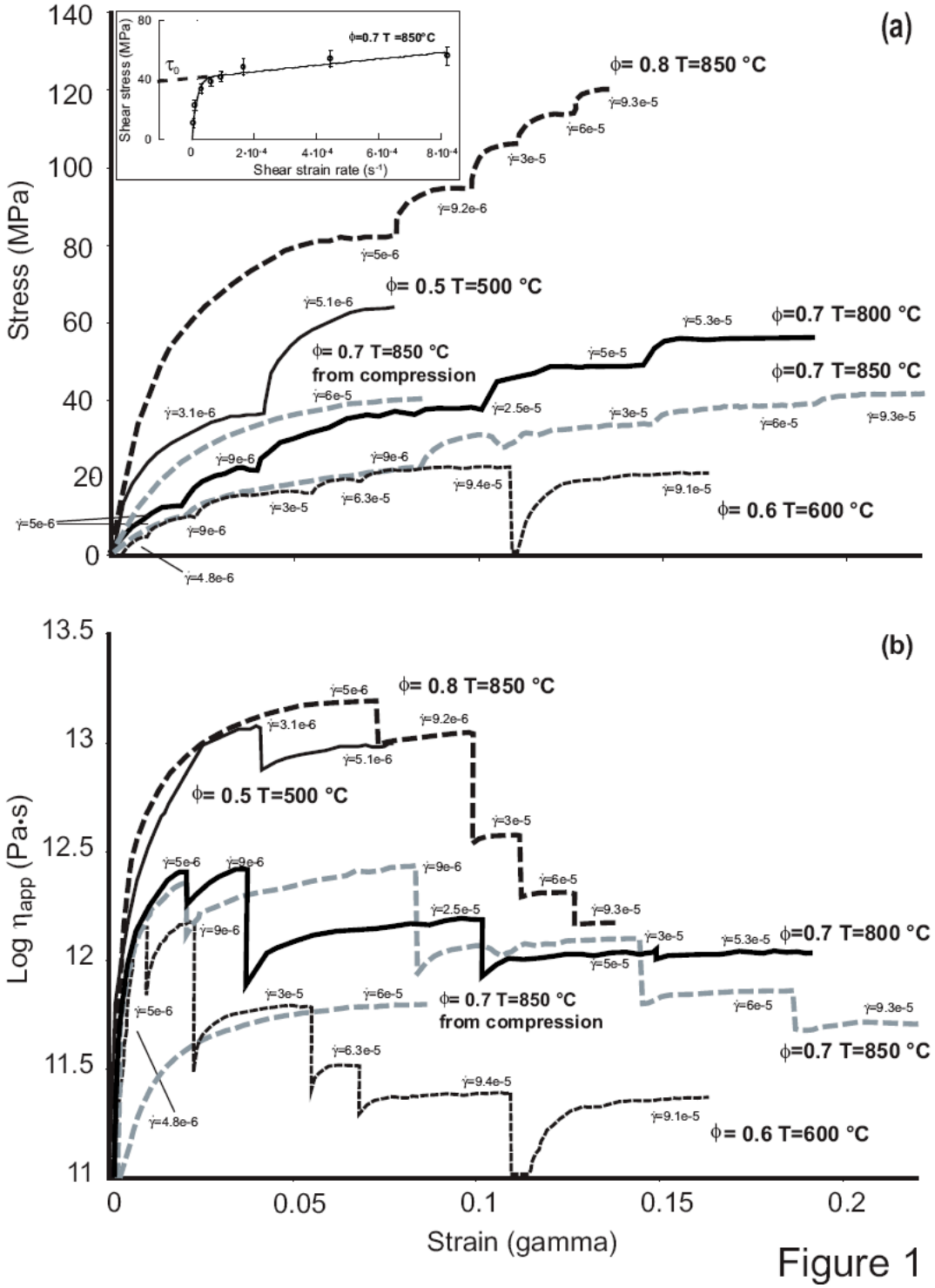

Figure 1

908

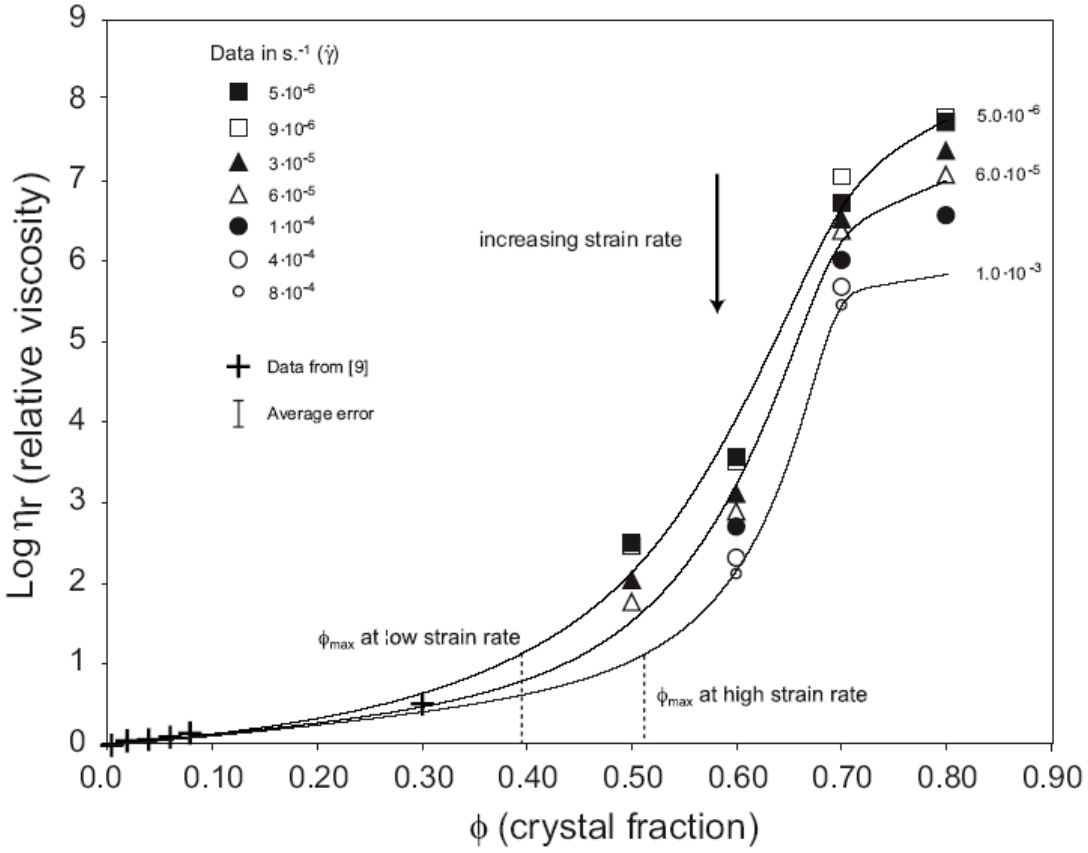

Figure 2

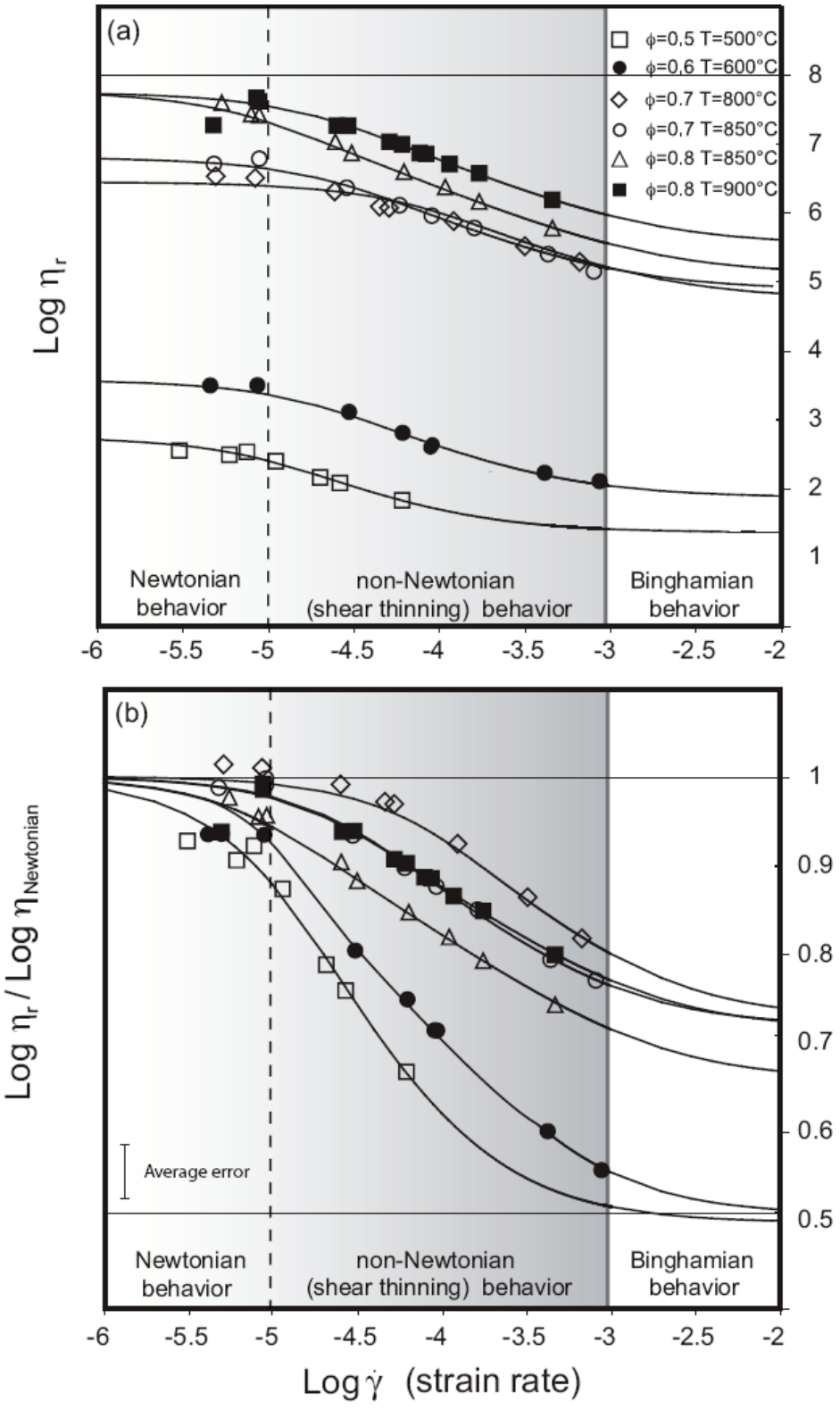

Figure 3

916

917

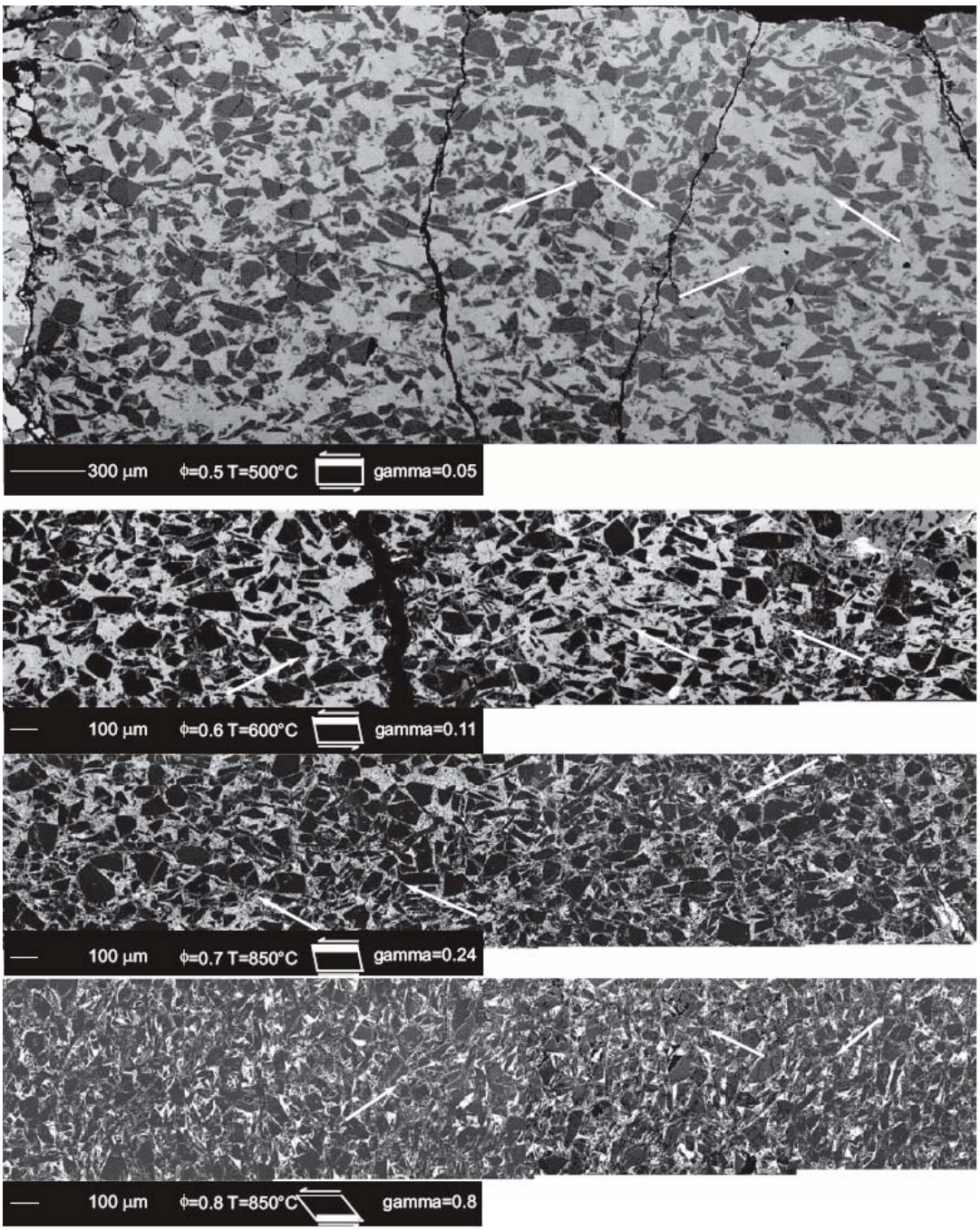

Figure 4

918

919

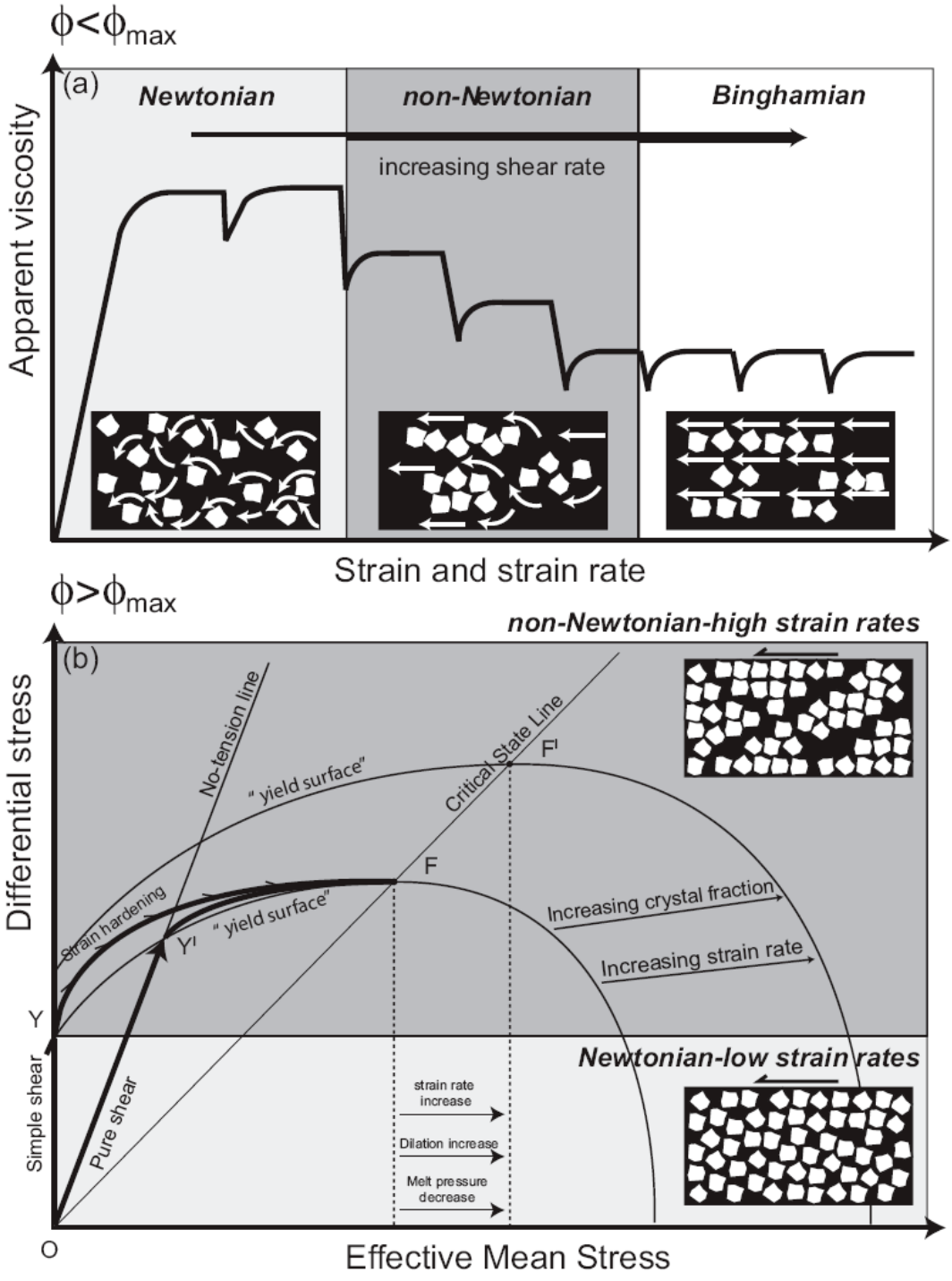

Figure 5

920

921

922

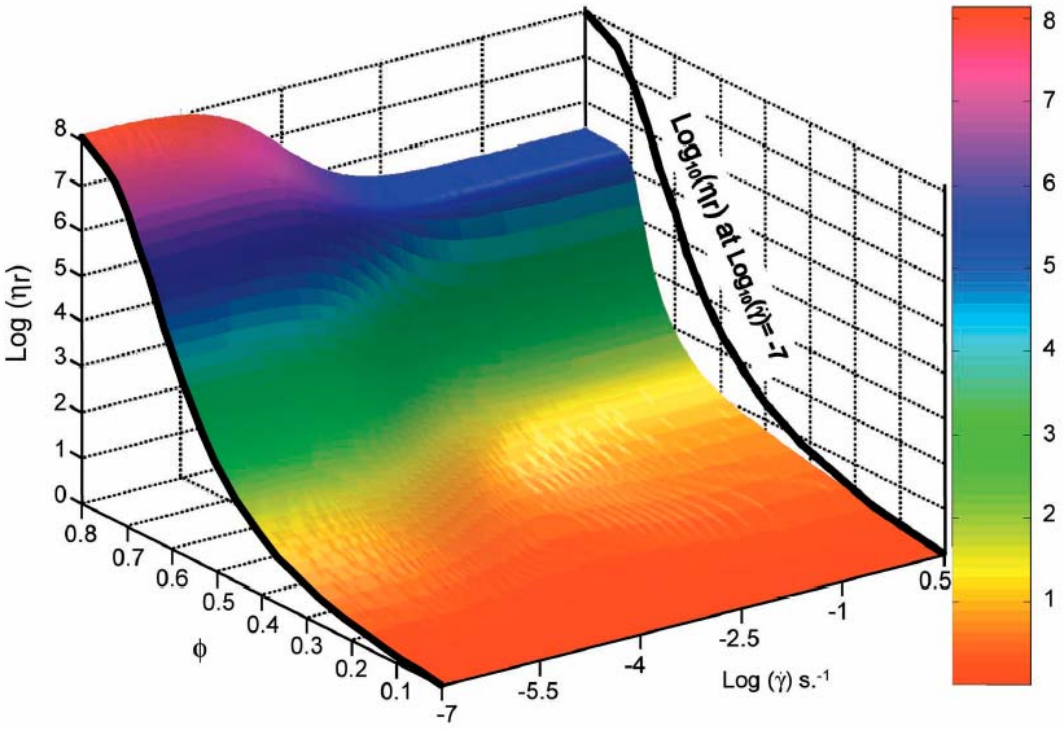

Figure 6

923

924

925

926

927

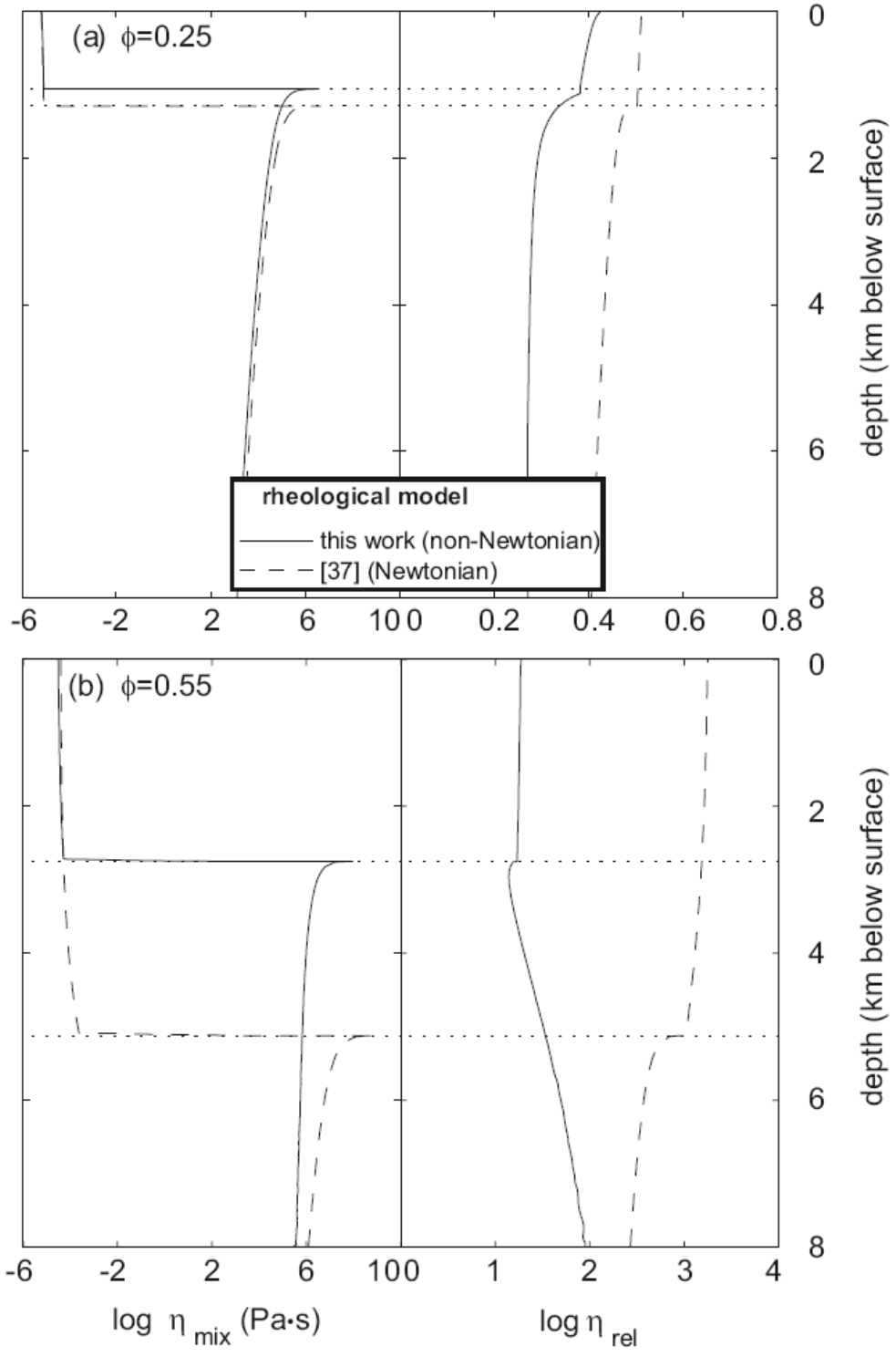

Figure 7

928

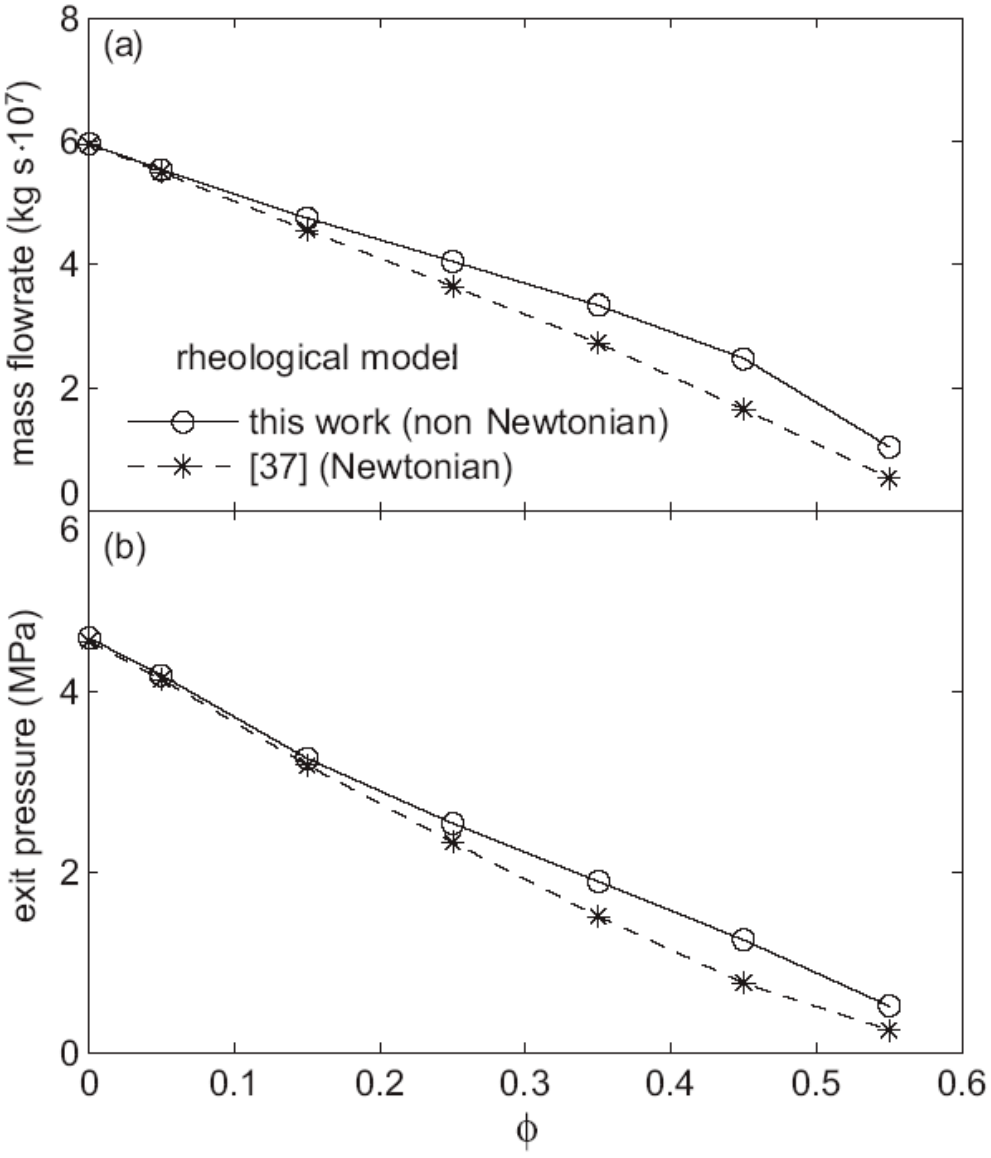
(a)
(b)
mass flowrate (kg s·10^7)
exit pressure (MPa)
rheological model
this work (non Newtonian)
[37] (Newtonian)
ϕ
0
2
4
6
8
0.1
0.2
0.3
0.4
0.5
0.6

Figure 8

929

930

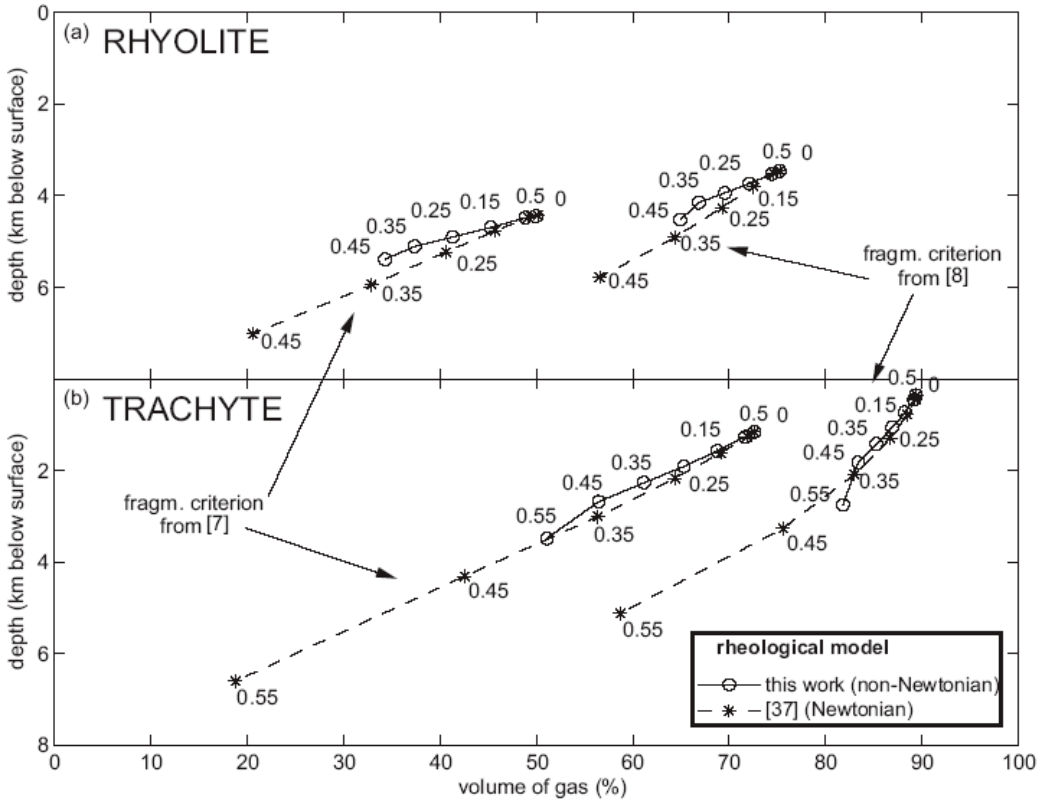

Figure 9

931